4.3 A 140GHz Transceiver with Integrated Antenna, Inherent-Low-Loss Duplexing and Adaptive Self-Interference Cancellation for FMCW Monostatic Radar

Xibi Chen[1], Muhammad Ibrahim Wasiq Khan[1], Xiang Yi[1,2], Xingcun Li[1,3], Wenhua Chen[3], Jianfeng Zhu[4], Yang Yang[4], Kenneth E. Kolodziej[5], Nathan M. Monroe[1], Ruonan Han[1]

[1]Massachusetts Institute of Technology, Cambridge, MA, [2]South China University of Technology, Guangzhou, China, [3]Tsinghua University, Beijing, China, [4]University of Technology Sydney, Ultimo, Australia, [5]MIT Lincoln Laboratory, Cambridge, MA

Sub-THz radars in CMOS are attractive in vital-sign and security sensing applications, due to their low cost, small size, and high resolution. Commonly used bistatic configuration, however, leads to serious beam misalignment between TX and RX, when large-aperture lenses/mirrors are used for longer range and higher spatial precision. As shown in [1], a 4mm physical separation between TRX antennas at 122GHz can cause 6° TRX beam misalignment, exceeding the 3dB beamwidth of the 29dBi-directivity beam. Monostatic radars are, therefore, preferred in those applications, when sufficient TRX isolation is achieved to avoid saturating the RX. Prior monostatic radars [2-6] adopt hybrid/directional couplers for passive TRX duplexing, but at the cost of 3dB+3dB insertion loss inherent to couplers. In [3], such extra loss is mitigated through two sets of hybrid couplers and a quad-feed circularly polarized antenna. Note that in all full-duplex systems, antenna interface mismatch degrades the TRX isolation; in [3], the achieved 26dB isolation relies on excellent antenna matching enabled by backside radiation through a silicon lens. In comparison, frontside radiation allows for low-cost packaging and pairing with compact, large aperture planar lens, but it causes much degraded antenna matching, hence is challenging for monostatic operation. In this paper, we present a 140GHz monostatic radar in CMOS, which not only circumvents the 6dB inherent insertion loss of couplers, but also facilitates the highly-desired frontside radiation through an adaptive self-interference cancellation (SIC), achieving 33.3dB of total TRX isolation.

The key technique for inherently lossless duplexing is illustrated in Fig. 4.3.1, where a turnstile antenna is driven by two feed ports V_1 and V_2. With a 90° delay line in the V_2 path, a common-mode excitation (V_1=V_2) creates a right-handed circularly polarized (RHCP) radiation in the TX mode. When reflected from the target, the wave received by the same antenna becomes left-handed circularly polarized (LHCP), inducing the same relative phase among the four antenna branches as in the TX mode. Interestingly, with the additional 90° delay in the V_2 path, the RX signal is in differential mode at the V_1 and V_2 ports (V_1=-V_2). Next, to redirect these two mode components to corresponding TX and RX circuits, a compact, dual-slot-based duplexer structure is adopted, where two identical slots are connected in shunt at the TX port and in series at the RX port. As Fig. 4.3.1 shows, signal injection at TX port leads to V_1=V_2, and the CPW-like field distribution in the two slots gives ideally zero leakage to the RX port. Next, when V_1=-V_2 (RX mode), the electrical potentials in the two slots are summed and extracted at the RX port, but are shorted at the TX port. The simulated TX-to-ANT and ANT-to-RX insertion loss, mainly due to metal resistance, are only 0.4dB and 1.6dB, respectively, while the TX-to-RX isolation with fully matched antenna ports is 34dB (Fig. 4.3.2). The combination of the duplexer and turnstile antenna then enables monostatic operation without 6dB coupler inherent loss. The adopted circular polarization also mitigates radar clutters caused by the second reflection at the ground, since double-reflection will generate the same RHCP wave and thus cannot be received by RX. Lastly, we note that the above isolation solely relies on structural symmetry of the duplexer; so even at extremely large sensing angles (not used in our case), where the wave degenerates to linear polarization, high isolation is still obtained, with only maximum 3dB more inherent ANT-RX insertion loss (Fig. 4.3.1). In simulation, the antenna axial ratio including the degradation from the duplexer structure is below 3dB within 20GHz bandwidth.

The on-chip turnstile antenna, shown in Fig. 4.3.2, is based on a crossed hollow bow-tie design, with a PCB metal reflector behind the 150μm-thick Si substrate. Compared to standard crossed dipole antennas, our design is broadband and the hollow structure minimizes both the blockage of the PCB-reflected wave to the frontside and the coupling to the feed lines, which increases the overall peak radiation efficiency from 19% to 32% (Fig. 4.3.2). To mitigate the isolation degradation caused by antenna mismatch and geometric asymmetry, additional transistors and MOS varactors are connected with the two duplexer slots (Fig. 4.3.2), serving as tunable mode-balancing devices. With proper differential bias tuning of these devices, a complex signal reflection at the duplexer ANT port is generated to cancel the TX-RX leakage within certain magnitude/phase ranges. Similar to that in [5], the tuning voltages are generated automatically through an adaptive SIC feedback control loop, where the low-pass-filtered RX baseband I-Q signals serve as the indicators for the leakage amplitude and phase. The SIC circuit blocks are given in Fig. 4.3.1. A VGA-based phase tuner is applied to arbitrarily control the sign and phase for the I-Q signals. A second-stage baseband amplifier with off-chip capacitive loads generates an open-loop gain of feedback that is large for low-IF leakage signal and small for the high-IF radar echo signals. Note that a one-time sign control and phase tuning are needed to ensure the negative feedback operation.

Fig. 4.3.3 shows the schematics of the RF building blocks. Two X8 multiplier chains are used to turn an input at ~17.5GHz to the TX and LO signals at ~140GHz. In both the TX and LO paths, 4-stage, two-way power amplifiers (PAs) with slot-based splitter/combiners are adopted, where each stage has a cross-coupled topology for neutralization. The smooth transitions from slot to GCPW in the splitters/combiners effectively reduces the insertion loss and thus lead to higher PA output power. In simulation, the TX chain has over 11dBm of output power across 18GHz bandwidth. The RX chain includes a low-noise amplifier (LNA) with two cascaded neutralized stages. The simulated gain, noise figure (NF) and $P_{in,1dB}$ of LNA including an input noise-matching balun is 11dB, 7.3dB and -6.5dBm, respectively. A trade-off between the LNA gain and its linearity is intentionally applied here, in order to conservatively protect the RX from saturation due to the potential TX to RX leakage. The output of the LNA is connected to two mixers for I-Q downconversion. Passive Gilbert mixer topology is chosen to avoid excessive flicker noise that disturbs the SIC loop and lowers the sensitivity. The simulated SSB NF of the LNA+mixer chain is 12dB. Lastly, shown in Fig. 4.3.1, in the I-Q IF paths, high-pass filters are inserted before the IF amplifiers for further suppression of the leakage at the IF outputs.

The chip is fabricated using a 65nm bulk CMOS technology. The chip can pair with a detachable planar lens with 39x39mm^2 size. Realized with 3D polymer and metal printing, the lens has 24x24 metasurface resonator units for local phase shifting. The measured peak EIRP, with and without the lens, is 9.8dBm and 25.2dBm, respectively. The measured lens-enhanced radiation patterns in Fig. 4.3.4 not only show sharp (~4°) beam profile, but also accurate TX and RX beam alignment enabled by the monostatic operation. Based on the measured radiation directivity and simulated radiation efficiency without the lens, we estimate that the total radiated TX power and the PA-generated power are 6.2dBm and 11.2dBm, respectively. Using the gain method, the measured minimum SSB NF with and without the antenna and duplexer loss is 20.2dB and 12.9dB, respectively. Both the measured TX and RX performances agree well with the simulations. Through the I-Q outputs of the open-loop SIC network, the TX-RX isolation enabled by the on-chip duplexer is 17~25dB across 14GHz bandwidth (Fig. 4.3.5). Under FMCW (BW=14GHz) operation with SIC turned on, 8.3dB suppression in the IF leakage spectrum (with f_{IF}<100kHz) is obtained, raising the overall isolation to 33.3dB. Fig. 4.3.5 also demonstrates the detection of a metal object 215cm away from the chip. Spurious tones that are close to the target peak and with ~10dB lower power are observed, due to nonlinear distortion of the generated FMCW signal from the off-chip DDS board (AD9164-FMCC-EBZ) and multiplier chain. The chip has an area of 3.1mm^2 and consumes 405mW of power. Lastly, a comparison with state-of-the-art monostatic radar chips is given in Fig. 4.3.6. This work achieves the highest total radiated power, and is the only one that simultaneously mitigates the 6dB inherent coupler loss and reaches >30dB isolation.

Acknowledgement:
The authors would like to thank Virginia Diodes Inc. (VDI) for the support of test instruments.

References:
[1] M. Pauli et al., "Miniaturized Millimeter Wave Radar Sensor for High Accuracy Applications," *IEEE T-MTT*, vol. 65, no. 5, pp. 1707–1715, 2017.
[2] M. Kucharski et al., "Monostatic and Bistatic G-Band BiCMOS Radar Transceivers With On-Chip Antennas and Tunable TX to RX Leakage Cancellation," *IEEE JSSC*, vol. 56, no. 3, pp. 899–913, 2021.
[3] J. Grzyb et al., "A 210–270GHz Circularly Polarized FMCW Radar With a Single Lens Coupled SiGe HBT Chip," *IEEE Trans. THz Sci. & Techn.*, vol. 6, no. 6, pp. 771–783, 2016.
[4] G. Pyo et al., "Single Antenna FMCW Radar CMOS Transceiver IC," *IEEE T-MTT*, vol. 65, no. 3, pp. 945–954, 2017.
[5] M. Kalantari et al., "A Single Antenna W-Band FMCW Radar Front End Utilizing Adaptive Leakage Cancellation," *ISSCC*, pp. 88–90, 2020.
[6] M. Hitzler et al., "On Monostatic and Bistatic System Concepts for mmWave Radar MMICs," *IEEE T-MTT*, vol. 66, no. 9, pp. 4204–4215, 2018.

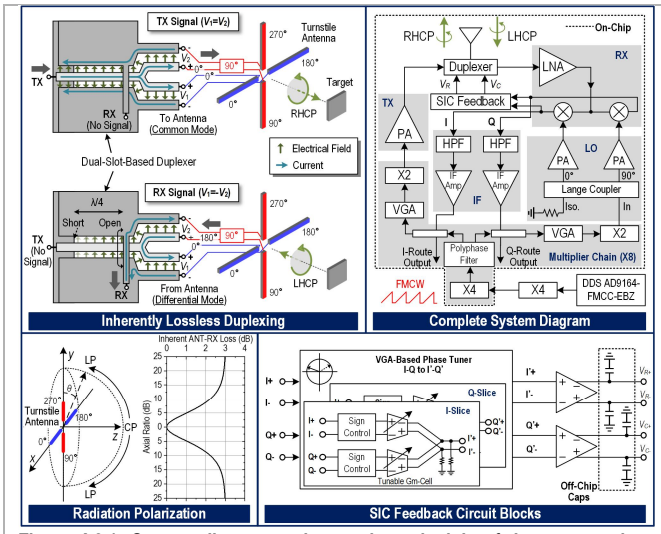

Figure 4.3.1: System diagram and operation principle of the monostatic radar transceiver chip.

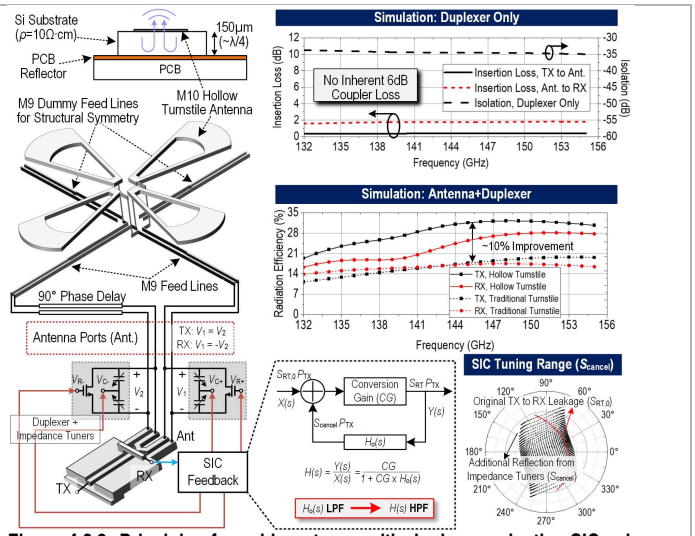

Figure 4.3.2: Principle of on-chip antenna with duplexer, adaptive SIC scheme, and simulated performances.

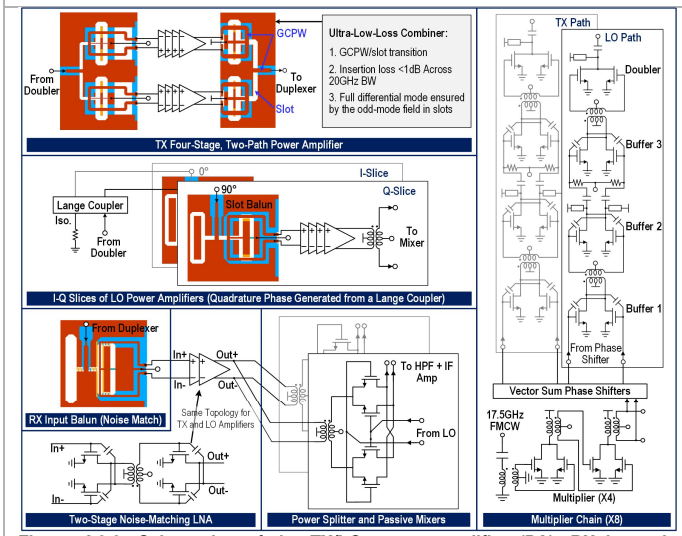

Figure 4.3.3: Schematics of the TX/LO power amplifier (PA), RX low-noise amplifier (LNA), passive mixer and input multiplier chain (X8).

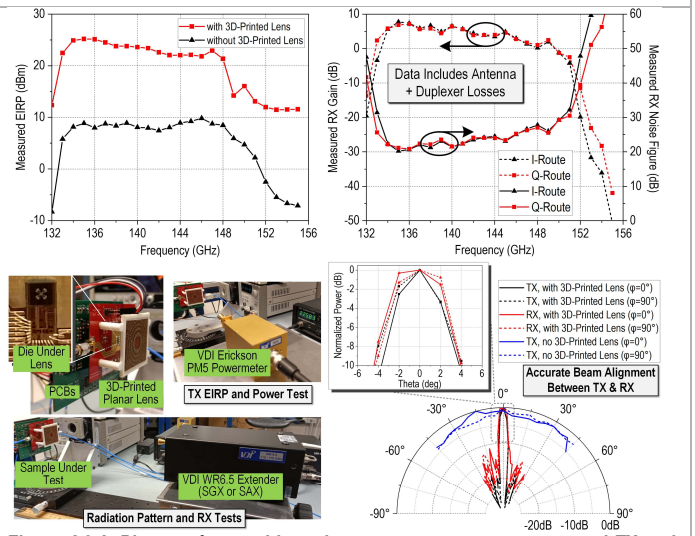

Figure 4.3.4: Photos of assembly and measurement setups, measured TX and RX performances, and radiation patterns of the radar transceiver chip.

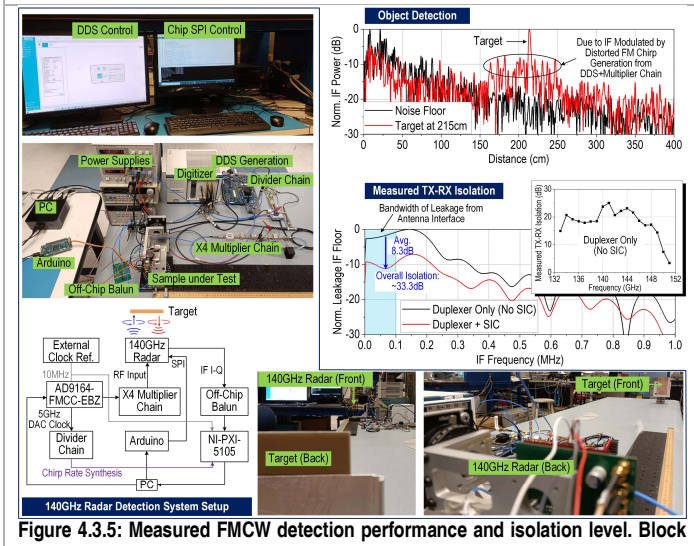

Figure 4.3.5: Measured FMCW detection performance and isolation level. Block digram and photos of the radar detection setup are also shown.

References	This Work	JSSC 2021 [2]	T-THz 2016 [3]	T-MTT 2017 [4]	ISSCC 2020 [5]	T-MTT 2018 [6]
Technology	65nm CMOS	130nm SiGe	130nm SiGe	130nm CMOS	65nm CMOS	130nm SiGe
Frequency (GHz)	134~148	160~178	210~270	23.8~24.5	80~85	150~170
Inherent 6dB Coupler Loss?	No	Yes	No	Yes	Yes	Yes
EIRP (dBm)	9.8, 25.2[a]	8	32.8[e]	N/A	17[g]	32[i]
TX Power (dBm)	11.2[b]	3	N/A	-1.6	2	3
Total Radiated Power (dBm)	6.2	N/A	5	N/A	N/A	N/A
RX NF_{min} (dB)	12.9	15.5	~19	11.6	15	20
Adaptive SIC	Yes	No	No	No	Yes	No
Isolation (dB)	33.3[c]	25	26	47.3[f]	40[h]	17
Antenna Type	On-Chip	On-Chip	On-Chip	Off-Chip	Off-Chip	Off-Chip
Radiation Direction & Antenna Feature	Front-Side with 3D-Printed Planar Lens	Back-Side with Substrate Etching[d]	Back-Side with Silicon Lens	Horn Antenna	4×8 Patch Antenna Array	Dielectric Resonator Antenna
Die Area (mm^2)	3.1	5.4	3.2	1.5	1	1.9
DC Power (mW)	405	860	1600~2000	111	120	N/A

(a) with 3D-printed lens (b) assuming 32% simulated antenna efficiency (c) under 14GHz-wide FMCW chirping
(d) localized backside etching (e) with silicon lens (f) achieved in a narrowband by manual impedance tuning
(g) with off-chip 4×8 patch antenna array (h) reported in a narrowband measurement
(i) with off-chip dielectric-resonator antenna

Figure 4.3.6: Comparison with state-of-the-art FMCW monostatic integrated radars.

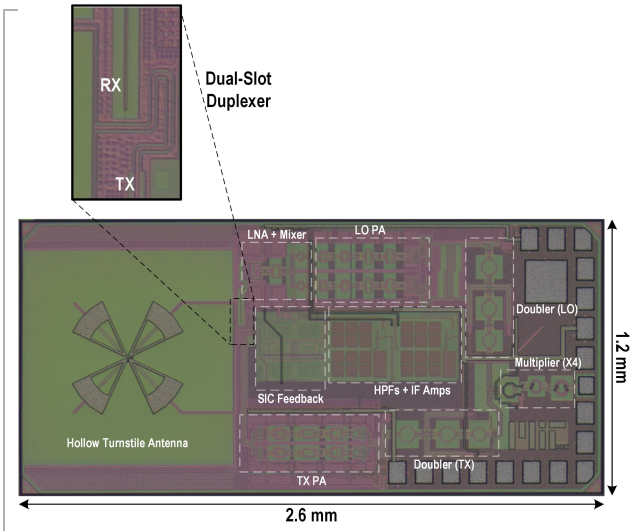

Figure 4.3.7: Die Micrograph.